ORIGINAL PAPER

Time-varying characteristics on migration and loss of fine particles in fractured mudstone under water flow scour

Luzhen Wang[1] · Hailing Kong[1] (ID) · Chengchun Qiu[1] · Bing Xu[1]

Abstract

It is very common in geotechnical engineering with Karst geological conditions that the fine particles migrate and lose continuously with water flow in the fractured rock mass, which will lead to the water-mud-inrush accident. In this paper, the time-varying characteristics of fine particles' migration and loss in fractured mudstone under water flow scour were investigated experimentally and theoretically. Considering the continuous gradation of fractured mudstone, taking Talbot power exponent as the influencing factor, the time-varying features of the total lost mass were described. Based on the total lost mass, the mass-loss rate and the mass-migration rate of fine particles were proposed, and their time-varying features were compared and analyzed. The loss-migration-ratio was defined, and the water-mud-inrush risk was assessed by the relationships between loss-migration-ratio and time. The research showed that (1) the lost mass resulted from the fine particles' migration, and the migrated mass was affected not only by lost fine particles but also by the water flow velocity. The rules of the fine particles' migration and loss in the fractured mudstone had the non-linear and time-varying characteristics. (2) For samples with the smaller Talbot power exponent of $n = 0.1$–0.5, the fine particles splashing phenomenon occurred, and quite a lot of migrated fine particles were lost. The loss-migration-ratio attenuated with time by a power function. Fractured mudstone with this continuous gradation had a high water-mud-inrush risk. (3) For samples with $n = 0.6$–1.0, large numbers of fine particles migrated with water flow, but only a few rushed out from the fractured mudstone. The loss-migration-ratio attenuated with time by an exponent function. Fractured mudstone with this continuous gradation had a stable inner structure; therefore, the water-mud-inrush risk was very low. The results will help geotechnical practitioners to assess the water-mud-inrush risk and provide some references for the water-mud-inrush accidents prevention in geotechnical engineering with Karst geological conditions.

Keywords Fractured mudstone · Fine particles · Migration and loss · Talbot power exponent · Mass-loss rate · Mass-migration rate

Abbreviations

a	The radius of the cylinder of the permeameter (L)
a_1, a_2, b_1, b_2	Coefficients (−)
d	The particle diameter of the current fractured mudstone (L)
D	The maximum particle diameter of fractured mudstone (L)
h	The loose height of the fractured mudstone in the cylinder (L)
m_{fp}/m_{fpi}	Mass of fine particles (M)
m_l	Total lost mass (M)
m_{li}	Total lost mass in the inrush mass loss stage (M)
m_{lf}	Final total lost mass (M)
m_{lr}	Total lost mass in the rapid mass loss stage (M)
M	Total mass of fractured mudstone (M)
M_d	Mass of fractured mudstone with particles diameters no greater than d (M)
n	Talbot power exponent (−)
$P(d)$	Percentage of the mass of the particle whose diameter is less than d (−)
P_{if}	The percentage that m_{li} accounts for m_{lf} (−)
P_{rf}	The percentage that m_{lr} accounts for m_{lf} (−)

✉ Hailing Kong
hailkong@126.com

1 College of Civil Engineering, Yancheng Institute of Technology, Yancheng 224051, Jiangsu, China

q_l/q_{li}	Mass-loss rate ($MT^{-1} L^{-3}$)
q_{lmax}	The maximum value of the mass-loss rate ($MT^{-1} L^{-3}$)
q_m/q_{mi}	Mass-migration rate ($MT^{-1} L^{-3}$)
q_{mmax}	The maximum value of the mass-migration rate ($MT^{-1} L^{-3}$)
q_s/q_{si}	Water flow scour rate ($MT^{-1} L^{-3}$)
t	Water flow time (T)
u_w	Water flow velocity (LT^{-1})
u_{fp}	Fine particles' migration velocity (LT^{-1})
V	Normal volume of the fractured mudstone at the loose state in the cylinder (L^3)
ρ_{fp}/ρ_{fpi}	Mass concentration of the fine particles in the pore of fractured mudstone (ML^{-3})
Δm_i	Mass of lost fine particles in the collection time Δt_i (M)
Δt_i	Collection time of the lost fine particles (T)
η	Loss-migration-ratio (−)

Introduction

The distribution of Karst geological conditions accounts for about one third of the total area in China. With the development of wide-long-deep tunnel construction, the accompanying water-mud-inrush accident has become one of the most common disasters in geotechnical engineering with Karst geological conditions (Qian 2012). Some water-mud-inrush accidents in Karst tunnels are listed in Table 1.

The accidents occurred frequently, which aroused the wide concern of scholars. The multi-factors evaluation methods (Li et al. 2013; Li et al. 2015a, b; Peng et al. 2016; Wang et al. 2016a, b, c, 2017a, b; Li et al. 2017a, b; Shi et al. 2018), fuzzy comprehensive evaluation methods (Li et al. 2011; Chu et al. 2017; Zhu et al. 2018), gray evaluation models (Zhou et al. 2015a, b; Yuan et al. 2016; Li and Yang 2018), mathematical theories (Yang and Zhang 2018), and mechanical-geology-mathematical models (Hao et al. 2018) were effectively proposed to forecast the accidents and provided scientific guidance for Karst tunnel

construction. However, these evaluation results did not describe the development and formation of water-mud-inrush in Karst tunnel.

It is worth noting that mud always inrushes with water in these accidents. In order to reflect the process of water-mud-inrush in Karst tunnel, many scholars studied the inrush process by establishing all kinds of coupled models by physical model experiments (Herman et al. 2009; Zhou et al. 2015a, b; Wang et al. 2016a, b, c; Liang et al. 2016; Wang et al. 2016a, b, c; Zhang et al. 2017; Yang et al. 2017; Li et al. 2017a, b; Pan et al. 2018; Zhao and Zhang 2018) and numerical simulation (Chu 2016; Li et al. 2016; Hu et al. 2018; Wu et al. 2017, 2018; Li et al. 2018 Liu et al. 2017a). Some large-scale and visual 3-D geologic model test systems were developed and established (Zhou et al. 2015a, b; Wang et al. 2016a, b, c; Zhang et al. 2017; Li et al. 2017a, b; Pan et al. 2018), they found that before the inrush of water and mud, and the mass of gushed particles decreases temporarily and then increases rapidly; the catastrophic process was divided into five stages—scattered tiny cracks, crack connection, water channels, water channels extension and transfixion, water inrush pathway—water inrush and mud gush presented when the internal displacement of filling increased, stress and seepage pressure dropped successively from bottom up. Liang divided the whole water inrush process into two periods—accumulating period and instability period—and believed that the water inrush in tunnel construction was the result of water-rock coupling interaction (Liang et al. 2016). Zhao divided the process of water-mud-inrush into several stages—preparation-seepage-unstable-stable stages of mud-water mixture outburst—and considered that excavation disturbance, high water pressure, and effect of erosion and corrosion of water were the key factors of the water-mud-inrush in fractured rock masses (Zhao and Zhang 2018). Chu simulated and analyzed the micro- and macro-evolution processes of the karst conduit water inrush disaster by RFPA and FLAC^{3D} (Chu 2016). Li established a fluid-solid coupling model for saturated broken rocks, calculated the stress field and seepage field of the surrounding rock by FLAC^{3D} and C++ program, and pointed out that because of the rock

Table 1 Details of some water-mud-inrush accidents in Karst tunnels (Hu-Rong-Xi 2009)

Accidents location	Water-inrush (m^3/day)	Mud-inrush (m^3)	The negative effects	Characteristics
DYS (DK1994 + 636)	4000~15,000	80	The tunnel was flooded, construction was interrupted.	(1) The amount of sediment in the water was up to 20%~30%; (2) a steady water flow would last for a long time; and (3) the accidents occurred accompanying with flushing and scattering
LT	30 (average)	1800		
YLS (DK354 + 450)	96,000~165,600	1300	Human casualty was caused, the work face was covered by inrushed mud and rock fragments.	
YLS (DK354 + 879)	72,000 (maximum)	6000		
YLS (DK361 + 746)	240,000	15,000		
YLS (3#)	145,000	4200		
YSG (DK124 + 602)	50,000	−[a]		

[a] It was reported that a lot of mud and sand inrush with water, but no exact data was recorded

particles loss in the pore space, new seepage channels formed when the fault was exposed, which led to the groundwater inrush accidents (Li et al. 2016). The process of karst water bursting was simulated by Fast Lagrangian Analysis of Continua combined with FLAC[3D], and the safety factor of fillings in karst was calculated (Hu et al. 2018). Li and his team probed the water flow characteristics after inrush using the FLUENT software and showed that the flow velocity and pressure nearby the working face without water inrush were both small; as the water-inrush velocity increased, the pressure and the flow velocity in the tunnels increased proportionately (Li et al. 2017a, b; Wu et al. 2017, 2018; Li et al. 2018).

It is no doubt that these researches revealed the causes and rules of the occurrence of Karst water-mud-inrush to some extent. The original hidden aquifer structure will be inevitably destroyed during the process of tunnel construction. The fractured rock mass in the Karst tunnel will connect the aquifer structure and form water-through passageways. The aquifer structure becomes a water source, and water flows in the fractured rock mass accompanying with mud and rock fragments' migration and loss, which may lead to the water-mud-inrush accident. However, the migration and loss rules of mud and rock fragments with water flow in the Karst tunnel were not mentioned basically in the above researches, which was bound to affect the risk of the Karst water-mud-inrush accidents.

Liu (Liu et al. 2017a, 2017b, 2018) pointed out that the behavior of particles' erosion and migration reflected the dynamic evolution of particle loss and water inflow in the fractured rock. The flow pattern in the evolution process was divided into the Darcy flow in the initial flow stage, Brinkman flow in the rapid flow stage, and Navier-Stokes pipe flow in the final flow stage. Due to the effect of particle migration, the flow properties might change from Darcy to non-Darcy flow, which was a key signal for water-mud-inrush, and initial porosity and water pressure were two main effect factors; particle starting velocity was a critical condition. However, there were no details for the internal reasons resulting from particles' migration and loss, and the continuous grading of fractured rock was not mentioned at all.

As we know, the content of particles in fractured rock directly influences the rules of migration and loss, which can lead to the water-mud-inrush. Under the action of the water flow scour, the fine particles migrate out from the fractured rock, which changes the internal pore structure and increases the porosity of the fractured rock. With enough space in the fractured rock, large numbers of fine particles take part in the migration, resulting in a large number of lost particles. Continuously, when the lost mass achieves a critical value, the water flow changes from seepage to pipe flow, and the seepage instability occurs, which is called water-mud-inrush accident in geotechnical engineering. Therefore, the fine

particles' migration leading to the loss in the fractured rock is an important reason for water-mud-inrush, and it has the time dependence. For that reason, studying the time-varying characteristics of fine particles' migration and loss in fractured rock under water flow scour is a basic work to prevent the water-mud-inrush accidents in geotechnical engineering with Karst geological conditions.

In this paper, we take the continuous graduation of fractured rock as the influencing factor, analyze the time-varying rules of fine particles' migration and loss based on the measured lost mass in the experiments to discuss the internal reasons of water-mud-inrush resulting from particles' migration and loss, and assess the risk.

Experimental process

A self-designed experimental system is used, which consists of four subsystems, a pore water pressure loading and controlling subsystem, an axial load loading and displacement controlling subsystem, a data acquisition analysis subsystem, and a fine particle migration and collection subsystem, as shown in Fig. 1. The permeameter in the fine particles' migration and collection subsystem is the core component (Wang et al. 2017a, b; Wang and Kong 2018; Kong and Wang 2018a, b).

As the mudstone is very common in the inrushed sediments in the water-mud-inrush accident, we take the fractured mudstone as the experimental samples. We collected the mudstone samples from Shanxi Province in China, and the initial strength was measured as 36.8 MPa. According to the American Society for Testing and Materials standard, the minimum diameter of a cylinder must be at least three times the maximum rock grain size for eliminating the size effect. So, when the fractured mudstone is sieved, we set the maximum mudstone size as 25 mm. The fractured mudstone is sieved into eight groups with their particle diameters as 0–2.5 mm, 2.5–5 mm, 5–8 mm, 8–10 mm, 10–12 mm, 12–15 mm, 15–20 mm, and 20–25 mm, as shown in Fig. 2.

Then, the fractured mudstone is mixed according to the Talbot continuous grading formula:

$$P(d) = \frac{M_d}{M} \times 100\% = \left(\frac{d}{D}\right)^n \times 100\% \qquad (1)$$

where $P(d)$ is the percentage of the particles mass whose diameter is less than d, M_d is the mass of fractured mudstone with particle diameter no greater than d, in grams; M is the total mass of fractured mudstone, in grams; d is the particle diameter of the current fractured mudstone, in millimeters; D is the maximum particle diameter of fractured mudstone, in millimeters; and n is the Talbot power exponent. In our tests, the values of Talbot power exponents are assigned as 0.1, 0.2, 0.3, 0.4, 0.5, 0.6, 0.7, 0.8, 0.9, and 1.0.

Fig. 1 Experimental system
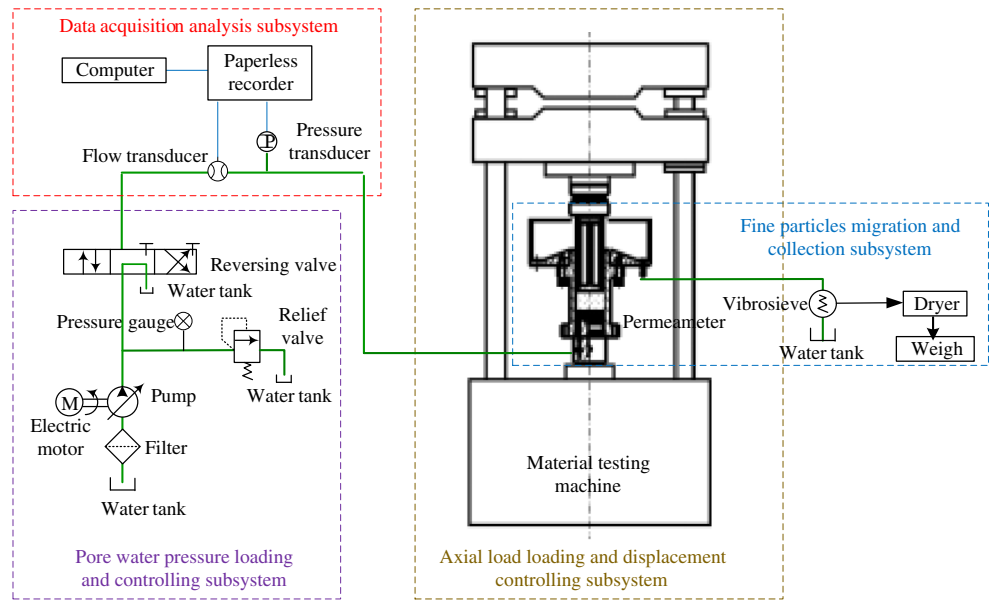
The mixed fractured mudstone sample is placed in the cylinder of permeameter at the loose state. The total mass of the sample, M, charged in the cylinder is 2000 g. According to Talbot power exponent, the mass of eight particles diameters groups for each sample is different, and the loose height, h, of each sample in the cylinder is different too. The mass is described in Fig. 3, and the loose height is shown in Table 2.

Ten sets of independent tests are required for 10 Talbot power exponents, and three samples for each set, so 30 samples are tested.

The test steps are explained clearly as below in Fig. 4. The continuous fine particles' migration and loss with water flow last for a long time. In order to master the fine particles' migration and loss rules in fractured mudstone completely, the testing time is longer than 18,000 s.

During every test, the pore pressure and the water flow will be monitored using the pressure transducers and the flow transducers in real time. The lost fine particles are separated from the turbidity water by the vibrosieve. Then, they are

collected, dried, and measured in a timely and stepwise manner by the filtration method, which is in a high frequency in the early test stage and then every 3600 s in the middle and late test stage.

The description of the fine particles' migration and loss

The fine particles refer to the fractured mudstone with diameters of no more than 2.5 mm in our tests. The mass of fine particles is m_{fp} in grams, which is different due to the Talbot continuous grading formula. The mass of fine particles decreases with the increasing Talbot power exponent as shown in Fig. 3. The large grains have the skeleton function, while the fine particles have the filling function. Because of the water flow scour, the fine particles migrate with water in the pore space among the large skeleton grains, some of them are rushed out with water, which is a long process.

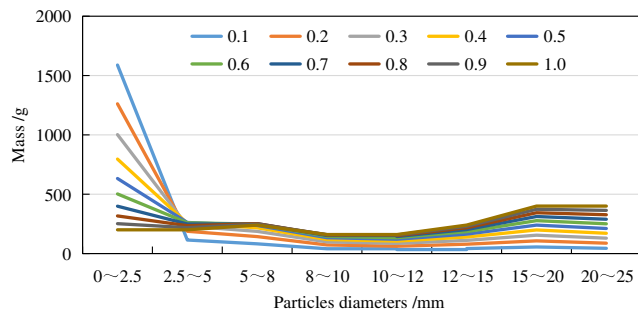**Fig. 2** Sieved fractured mudstone in eight particles diameters groups
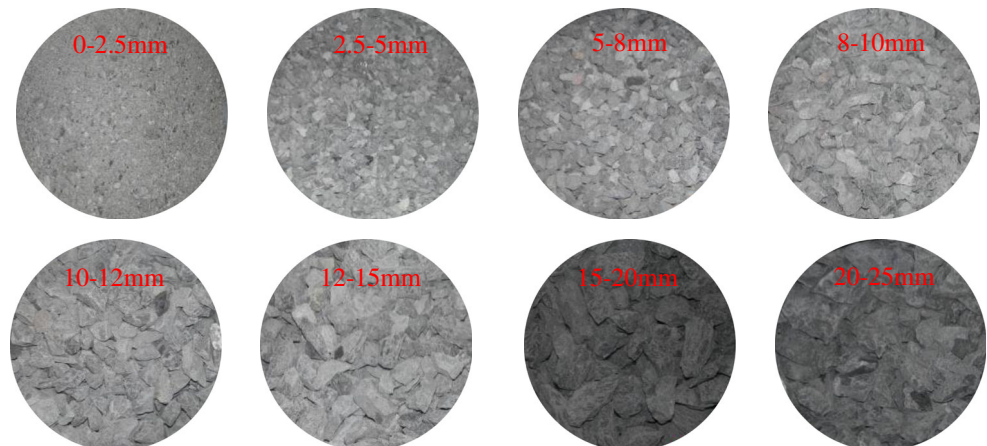
Fig. 3 The mass of eight particles diameters groups corresponding to ten Talbot power exponents

Fig. 4 Test steps

The mass-loss rate

If the mass of lost fine particles is $\Delta m_i = (i = 1, 2, 3, \cdots, n)$, corresponding collection time is $\Delta t_i = (i = 1, 2, 3, \cdots, n)$; obviously, the total lost mass in the fractured mudstone sample during each time period is

$$m_l = \sum \Delta m_i \tag{2}$$

The mass-loss rate, q_{li}, can be calculated as follows:

$$q_{li} = \frac{\Delta m_i}{V \Delta t_i} \tag{3}$$

where V is the normal volume of the fractured mudstone at the loose state in the cylinder, in cubic meters; it can be calculated by the formula below:

$$V = \pi a^2 h \tag{4}$$

in which a is the radius of the cylinder of the permeameter, in meters, and h is the loose height of the fractured mudstone in the cylinder, in meters.

Hence, the time-varying features of the mass-loss rate, q_{li}, can easily be obtained by the experiment.

The mass-migration rate

In this paper, the action of water flow scour only refers to the effect of water flow on the transport of fine particles, and the effect of water flow on the breakage of the fractured mudstone surface and on the reproduction of fine particles is not taken into consideration.

If the mass concentration of the fine particles in the pore of fractured mudstone is ρ_{fp}, the migration velocity is $\overrightarrow{u}_{fp}$, then
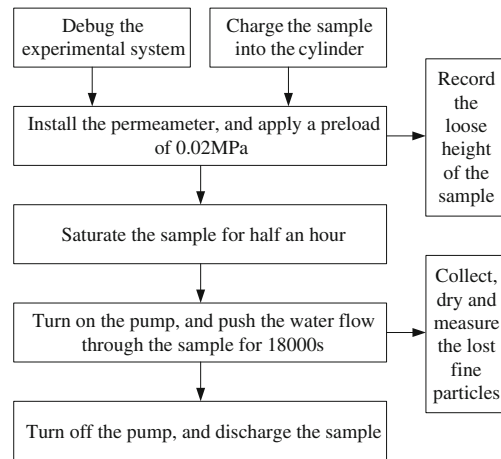
the water flow scour rate, q_s, can be deduced by Gauss divergence formula (Wang and Kong 2017) as follows:

$$q_s = \mathrm{div}\left(\rho_{fp}\overrightarrow{u}_{fp}\right) \tag{5}$$

In the simplified one-dimension problem, the Gauss divergence formula can be expressed as

$$\mathrm{div}\left(\rho_{fp}u_{fp}\right) = \rho_{fp}\frac{\partial u_{fpx}}{\partial x} \tag{6}$$

Supposed that there is no relative motion between the fine particles and the water flow when the fine particles start to migrate, the fine particles' migration velocity, u_{fp}, can be expressed as follows:

$$u_{fp} = u_w \tag{7}$$

in which, u_w, is the water flow velocity.

The real-time mass concentration of the fine particles in the pore of fractured mudstone, ρ_{fpi}, can be expressed as follows:

$$\rho_{fpi} = \frac{m_{fpi}}{V} \tag{8}$$

where m_{fpi} is the real-time mass of the fine particles in the fractured mudstone, in grams, which will be varied in time because of the fine particles' loss. It is

$$m_{fpi} = m_{fp} - \sum \Delta m_i \tag{9}$$

The corresponding real-time water flow scour rate, q_{si}, is

$$q_{si} = \frac{m_{fp} - \sum \Delta m_i}{\pi a^2 h}\frac{\partial u_w}{\partial x} \tag{10}$$

Table 2 The loose height corresponding to ten Talbot power exponents

Talbot power exponent (n)	0.1	0.2	0.3	0.4	0.5	0.6	0.7	0.8	0.9	1.0
The loose height (h)/mm	147	150	153	155	156	160	163	166	170	172

Because we have supposed that the fine particles' migration velocity approximately equals to the water flow velocity, the water flow scour rate, q_{si}, is just the mass-migration rate, q_{mi}, of the fine particles.

Approximate thought that the water flow is a steady flow in the fractured mudstone, and the height of the sample keeps the original height during the water flow. The mass-migration rate of the fine particles is expressed as

$$q_{mi} = \frac{(m_{fp} - \Sigma \Delta m_i) u_w}{\pi a^2 h^2} \tag{11}$$

Obviously, the mass-migration rate, q_{mi}, varies in time and relates to the water flow velocity.

Experimental results and analysis

The time-varying characteristics of the total lost mass

Lost fine particles can be measured directly in the test. According to Eq. (2), the total lost mass, m_l, can be calculated. Figure 5 shows the time-varying characteristics of the total

lost mass. The curves are much flatter in greater Talbot power exponents than that in smaller Talbot power exponents.

From Fig. 5, it is clear that the time-varying characteristics of the total lost mass are different between the samples of $n = 0.1$–0.5 and the samples of $n = 0.6$–1.0. There are three stages in the curves of $n = 0.1$–0.5, namely the inrush mass loss stage from 0 s to 20s, the rapid mass loss stage from 20 to 7200 s, and the slow mass loss stage from 7200 to 18,000 s. But, there are only two stages in the curves of $n = 0.6$–1.0, namely the rapid mass loss stage from 0 to 7200 s and the slow mass loss stage from 7200 to 18,000 s.

For samples with $n = 0.1$–0.5, there are a large number of fine particles in the fractured mudstone sample, and there will be much more in the smaller Talbot power exponent samples; even it accounts for 80% of the total mass when $n = 0.1$. When the pump is opened, the easily migrated fine particles are splashed with water flow in the first 20 s, and the splashed fine particles are of great many, and the lost speed is fast. Correspondingly, it is presented as the inrush mass loss stage when the time-varying curves increased sharply, and the vibration phenomenon of permeameter would be observed in the tests in this stage. Occasionally, in the instant of flushing, few particles larger than 2.5 mm were splashed out. After this inrush mass loss stage, the pore space becomes larger, and
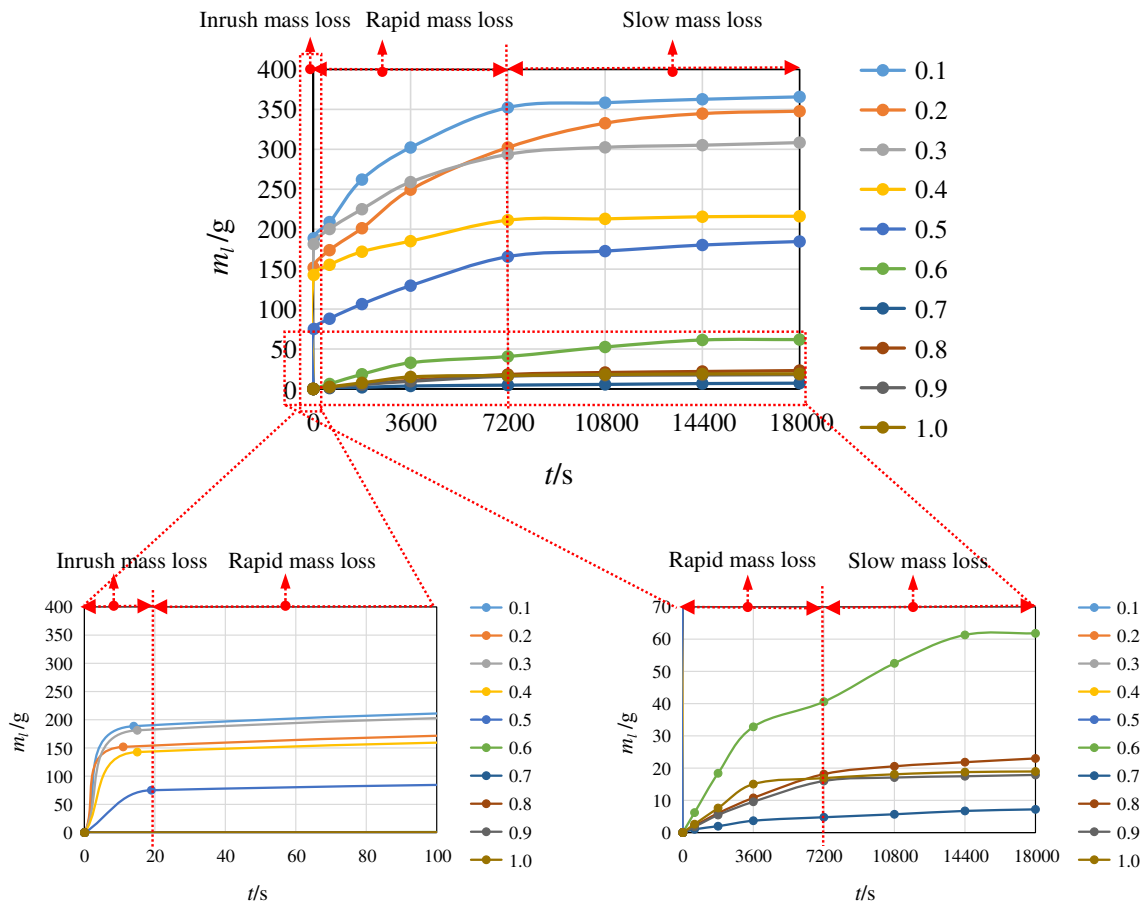

Fig. 5 The total lost mass varies in time

some fine particles are rushed out continuously and smoothly from 20 to 7200 s, which performs a rapid mass loss stage in the curves.

However, for samples with $n = 0.6$–1.0, with the increasing Talbot power exponents, the loose heights are higher as shown in Table 2. A small number of fine particles filled in the large skeleton grains, which forms a larger pore space in the samples. When the pump is opened, there is no fine particles spay out, but some migrate out smoothly from the sample. The curves perform the rapid mass loss stage.

After the rapid mass loss stage, the fine particles that migrate with water flow last for a longer time, and the amount of the fine particles that migrated out from the fractured mudstone is much less because of the relatively balanced structure in the sample. The curves perform a slow mass loss stage for samples with $n = 0.1$–0.5 and $n = 0.6$–1.0.

The total lost mass in the inrush mass loss stage, the total lost mass in the rapid mass loss stage, and the final total lost mass are expressed symbolically as m_{li}, m_{lr}, and m_{lf}, respectively. The percentage that m_{li} accounts for m_{lf} and the percentage that m_{lr} accounts for m_{lf} are expressed symbolically as P_{if} and P_{rf}, respectively. Table 3 shows the mass and the percentage.

It can be seen in Table 3 that the percentages, P_{if}, for samples $n = 0.1$–0.5 have an average value of 52%. This large value comes from the splashed fine particles in the permeameter, and it may change the water flow state in the fractured mudstone from seepage to pipe flow. This phenomenon is dangerous for a water-mud-inrush accident in geotechnical engineering.

It also shows from Table 3 that the percentage, P_{rf}, is closely related to the Talbot power exponent. Generally, the samples with Talbot power exponents of $n = 0.1$–0.5 have a higher percentage, and the average value is about 93%. While the samples with Talbot power exponents of $n = 0.6$–1.0 have a lower percentage of about 78% averagely.

There are a large number of fine particles in the samples with smaller Talbot power exponents of $n = 0.1$–0.5. In the beginning, the easily migrated fine particles transfer fast with water under the pore pressure. The amounts of the lost mass in this rapid mass loss stage are large, so the percentage of which account for the final total lost mass is higher. On the contrary, there are not enough fine particles in the samples with Talbot power exponents of $n = 0.6$–1.0, the fine particles migrate slowly under the pore pressure, and the pore structures are stable; therefore, even in the rapid mass loss stage, the lost mass is less, and the splashing does not happen.

The time-varying characteristics of the mass-loss rate

According to Eq. (3), the mass-loss rate can be calculated. Figures 6 and 7 show the time-varying characteristics of the mass-loss rate when $n = 0.1$–0.5 and $n = 0.6$–1.0, respectively.

In Fig. 6, the time-varying curves are divided into the sharp decline stage (0–20 s), rapid decline stage (20–7200 s) and slow decline stage (7200–18000 s) for the samples with $n = 0.1$–0.5. And, in Fig. 7, the curves are divided into the gradual decline stage (0–7200 s) and slow decline stage (7200–18000 s) for the samples with $n = 0.6$–1.0. Sometimes, there is a little growth in the decline stages for the samples of $n = 0.4$, $n = 0.7$, and $n = 0.9$. Maybe it comes from the pore structure adjustment.

The contents of the fine particles in fractured mudstone samples with $n = 0.1$–0.5 are large. When the pump is opened, lots of fine particles splash in a very short time under the pore pressure, the mass-loss rate achieves its maximum, and the magnitude is up to 10^4 g s^{-1} m^{-3}, as seen in Fig. 6. After the splashing, the magnitude is down to 10^1 g s^{-1} m^{-3}, which shows the sharp decline in the curve. As the time goes from 20 to 7200 s, the easily migrated fine particles become less and less, the lost mass becomes less correspondingly, and the magnitude of the mass-loss rate is about 10^0 g s^{-1} m^{-3}, which shows the rapid decline in the curve. The slow decline stage corresponds to the magnitude range from 10^0 to 10^{-1} g s^{-1} m^{-3}, and this stage lasts for a long time from 7200 to 18,000 s. In this stage, the decline of the mass-loss rate is more and more slowly.

In Fig. 7, there is no phenomenon of splashing during the whole experiment for samples with $n = 0.6$–1.0. Accompanying with less lost fine particles, there is only an adjustment between the migrated fine particles and the large skeleton grains in fractured mudstone. The magnitude of the mass-loss rate changes from 10^0 to 10^{-1} g s^{-1} m^{-3} during this adjustment process, corresponding to the gradual decline stage from 0 to 7200 s. In the slow decline stage, the magnitude keeps basically in 10^{-1} g s^{-1} m^{-3} in a long time from 7200 to 18,000 s. Sometimes, the magnitude drops to 10^{-2} g s^{-1} m^{-3} for samples with $n = 0.9$–1.0.

Table 3 The total lost mass in different stages and the percentages

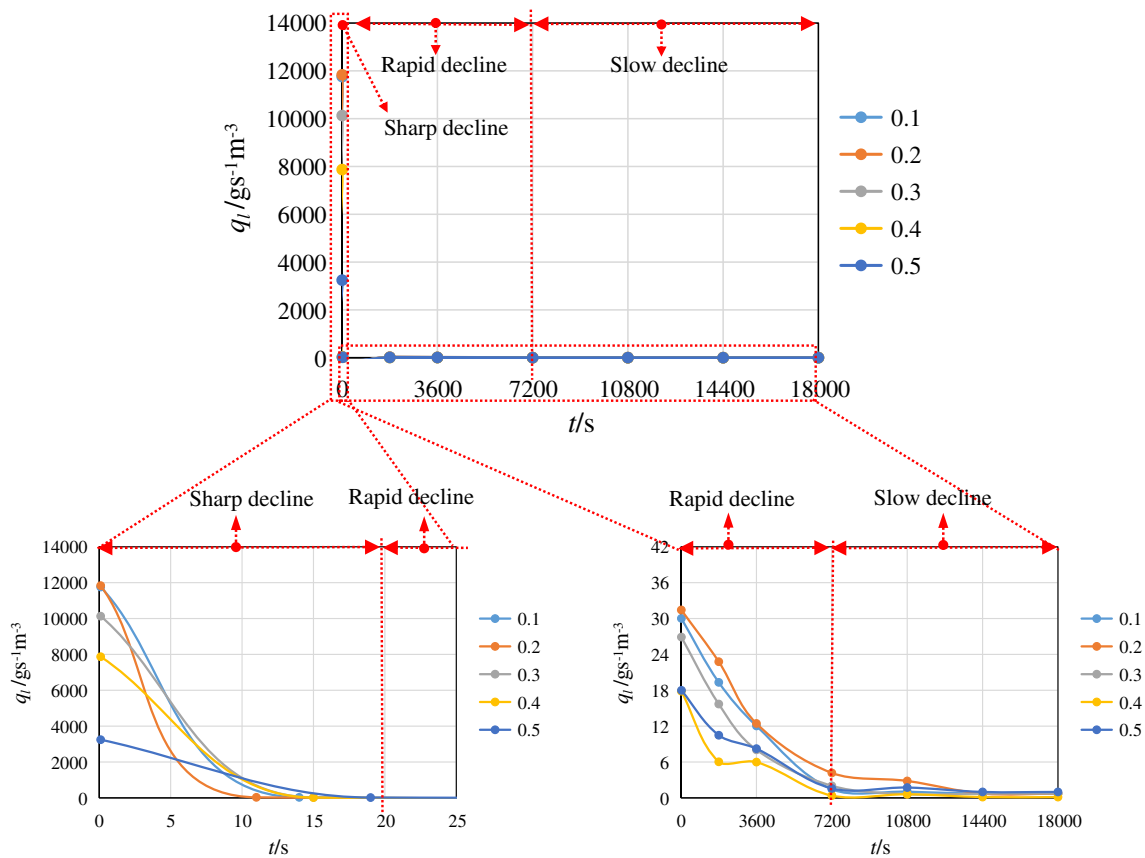| n	0.1	0.2	0.3	0.4	0.5	0.6	0.7	0.8	0.9	1.0
m_{li} (g)	188.6	151.9	181.3	142.7	75.1	–	–	–	–	–
m_{lr} (g)	352.2	302.2	293.7	211.3	165.6	40.6	4.76	18.1	16.0	16.9
m_{lf} (g)	365.6	347.7	308.4	216.2	184.6	61.8	7.2	23	17.9	19.0
P_{if} (%)	52%	44%	59%	66%	41%	–	–	–	–	–
P_{rf} (%)	96%	87%	95%	98%	90%	66%	66%	79%	89%	89%

Fig. 6 The mass-loss rate varies in time for samples with $n = 0.1$–0.5

The maximum values of the mass-loss rate, $q_{l\max}$, with different Talbot power exponents, n, are listed in Table 4.

It can be deduced that the maximum value of the mass-loss rate is determined by the total lost mass in the inrush mass loss stage for samples of $n = 0.1$–0.5, and the rapid mass loss stage for samples of $n = 0.6$–1.0. The samples with $n = 0.1$–0.5 have greater lost mass and shorter inrush mass loss stage duration; thus, they have the larger mass-loss rates, the maximum value even achieves 1.18×10^4 g s^{-1} m^{-3}. For samples with $n = 0.6$–1.0, because of the less lost mass and longer rapid mass loss stage duration, the maximum value of the mass-loss rate is only 8.22 g s^{-1} m^{-3}.
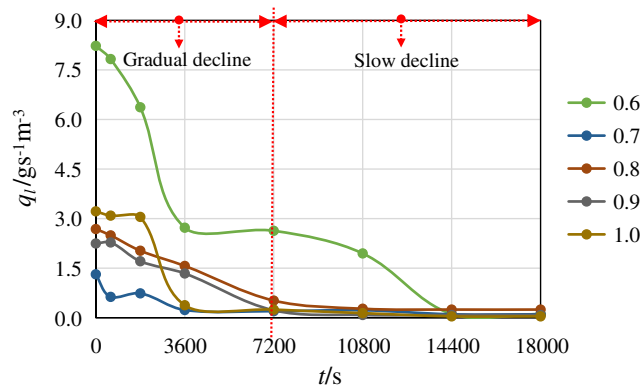

Fig. 7 The mass-loss rate varies in time for samples with $n = 0.6$–1.0

The time-varying characteristics of the mass-migration rate

According to Eq. (11), the mass-migration rate can be calculated. Figures 8 and 9 show the time-varying characteristics of the mass-migration rate when $n = 0.1$–0.5 and $n = 0.6$–1.0, respectively.

In Fig. 8, there are a rapid decline stage from 0 to 20s and a slow decline stage from 20 to 18,000 s. It is considered to be a dynamic pore pressure that when the pump is opened, a large number of fine particles are scoured by water flow, resulting in the migration. In the first 20 s, the migrated fine particles are so many that the mass-migration rate is great. After the first 20 s, the pore structure becomes stable gradually, and the scouring effect of the water flow becomes stable, too. Because of the continuous particle loss, the migrated fine particles become less after a long time, so the mass-migration rate performs a slow decline stage.

In Fig. 9, the mass-migration rate performs a slow decline tendency throughout. There are much larger skeleton grains and relatively less filling fine particles in the samples with larger Talbot power exponents. There is enough pore space among the large skeleton grains for the fine particles to migrate, and the migrated fine particles transfer with water flow in a stable state. As the fine particles migrate out from the

Table 4 The maximum values of the mass-loss rate with different Talbot power exponents (g s^{-1} m^{-3})

n	0.1	0.2	0.3	0.4	0.5	0.6	0.7	0.8	0.9	1.0
$q_{l\max}$	1.18×10^4	1.18×10^4	1.01×10^4	0.79×10^4	0.32×10^4	8.22	1.31	2.68	2.25	3.22

fractured mudstone continuously, the migration mass in the later test process is much less than it in the early process, so the mass-migration rate has a decline change.

The magnitude of the mass-migration rate decreases only from 10^5 to 10^4 g s^{-1} m^{-3} with the increased Talbot power exponent. It is because the mass-migration rate is not only related to the lost mass, but also related to the water flow velocity. The effect of velocity on the mass-migration rate is larger than that of lost mass.

The maximum values of the mass-migration rate, $q_{m\max}$, with different Talbot power exponents, n, are listed in Table 5.

Compared Tables 4 and 5, for samples with $n = 0.1$–0.5, the mass-migration rate is only 10 times larger than the mass-loss rate, it is deduced that quite a lot of migrated fine particles are lost. However, for $n = 0.6$–1.0, the mass-migration rate is nearly 10^4 times larger than the mass-loss rate; it is deduced that large numbers of fine particles migrate with water flow, but only a few are migrated out from the fractured mudstone.

The relationships between loss-migration-ratio and time

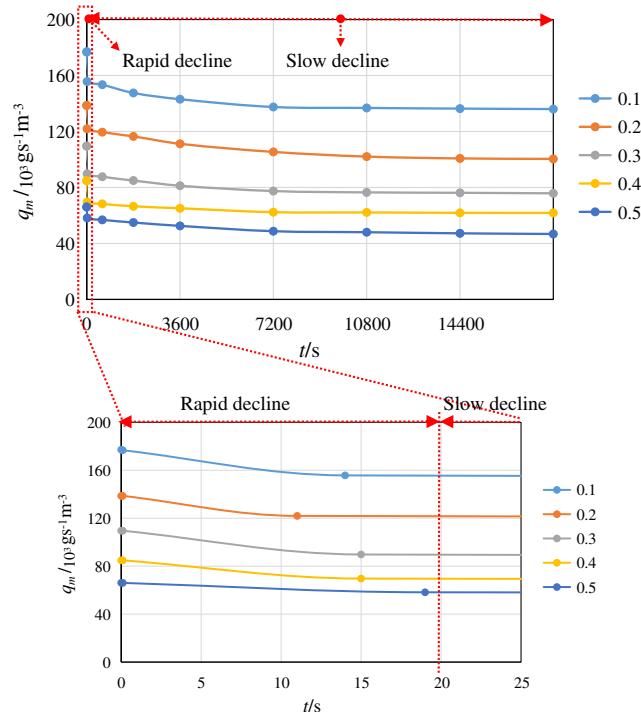There is particle migration in fractured rock mass under water flow scour, which causes the structural change of fractured rock mass, and migration is not the decisive factor of seepage stability, the amount of loss in migrating particles is the one. Therefore, the mass-loss rate and the mass-migration rate are used to define a physical quantity to describe the amount of loss in migrating particles, and it also could be used as a factor to assess the risk of water-mud-inrush accidents.

The loss-migration-ratio, η, is defined and calculated as below.

$$\eta = \frac{q_l}{q_m} \tag{12}$$

Obviously, the loss-migration-ratio is affected by Talbot power exponent and varies in time. As time goes on, the faster it decays, the larger the proportion of loss to migration; the more likely seepage instability happens, the higher the risk of water-mud-inrush accidents is, and vice versa.

Figure 10 shows the time-varying features of the loss-migration-ratio. It can be fitted by the functions in Table 6.

The loss-migration-ratio varies in time as a power function when $n = 0.1$–0.5, and it is an exponent function when $n = 0.6$–1.0. They are expressed in generic forms as:

$$\eta = a_1 t^{b_1}, (n = 0.1-0.5) \tag{13}$$

$$\eta = a_2 e^{b_2 t}, (n = 0.6-1.0) \tag{14}$$

where coefficients a_1, b_1, a_2, and b_2 are the functions of Talbot power exponent, n, and can be calculated from the following equations:

$$a_1 = -0.071n^2 + 0.043n + 0.004 \ (n = 0.1-0.5) \tag{15}$$

$$b_1 = 1.800n^2 - 0.968n - 0.586 \ \ (n = 0.1-0.5) \tag{16}$$

$$a_2 = 0.0031n^2 - 0.0049n + 0.0020 \ \ (n = 0.6-1.0) \tag{17}$$

$$b_2 = -0.0026n^2 + 0.0040n - 0.0017 \ \ (n = 0.6-1.0) \tag{18}$$

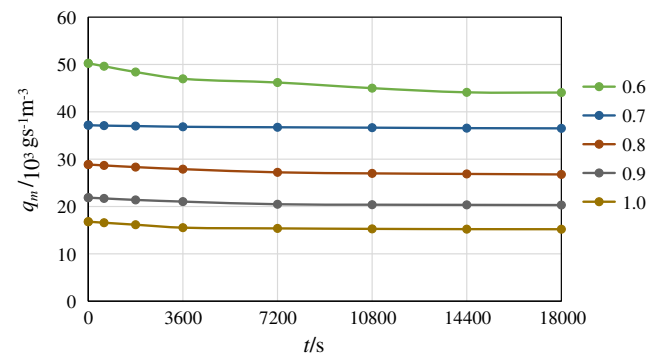**Fig. 8** The mass-migration rate varies in time for samples with $n = 0.1$–0.5

Fig. 9 The mass-migration rate varies in time for samples with $n = 0.6$–1.0

Table 5 The maximum values of the mass-migration rate with different Talbot power exponents ($\times 10^5$ g s^{-1} m^{-3})

n	0.1	0.2	0.3	0.4	0.5	0.6	0.7	0.8	0.9	1.0
$q_{m\mathrm{max}}$	1.18	1.39	1.10	0.85	0.66	0.50	0.37	0.29	0.22	0.17

Obviously, for samples with different Talbot power exponents, the loss-migration-ratio has different relationships with time. When the samples have higher contents of small and fine particles, the loss-migration-ratios of the samples attenuate fast with time. Fractured mudstone mass similar to this continuous gradation has a higher risk of water-mud-inrush at the beginning of the water flow in geotechnical engineering with Karst geological conditions. On the contrary, the loss-migration-ratios of the samples with much higher contents of large skeleton grains present a slow time-dependent attenuation. For fractured mudstone mass like this continuous gradation, the possibilities of water-mud-inrush accidents are very small in geotechnical engineering with Karst geological conditions.

Combining the time-varying characteristics of the total lost mass, the mass-loss rate, the mass-migration rate, and the loss-migration-ratio, it can be found that the water flow system in

the fractured mudstone has the non-linear and time-varying characteristics because of the fine particles' migration and loss. We consider that the migrated fine particles have the same velocity as the water flow and get the rules of fine particles' migration from quantity, rather than only observing and speculating in experiments. This research can provide references to forecast and prevent the water-mud inrush accidents in tunnel construction experimentally and theoretically.

Conclusions

The water flows in the fractured mudstone have the non-linear and time-varying characteristics because of the fine particles' migration and loss, which may lead to water-mud-inrush accidents in geotechnical engineering with Karst geological conditions. To study the rules of fine particles' migration and loss is the basis for researching the water-mud-inrush mechanism.

The rules of fine particles' migration and loss are different in the fractured mudstone due to the Talbot power exponent. For the smaller Talbot power exponents of $n = 0.1–0.5$, the splashing phenomenon can be observed in tests, and a large
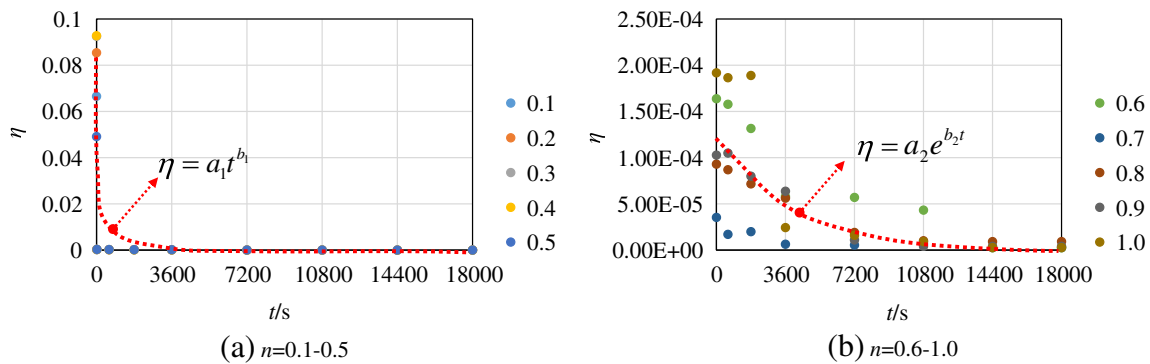

Fig. 10 The two different variations in time of the loss-migration-ratio ($n = 0.1–0.5$ & $n = 0.6–1.0$)

Table 6 The relationships of the loss-migration-ratio varying in time

Talbot power exponent (n)	Fitting function	Correlation coefficient
0.1	$\eta = 0.008 t^{-0.699}$	0.882
0.2	$\eta = 0.0086 t^{-0.647}$	0.872
0.3	$\eta = 0.0107 t^{-0.689}$	0.905
0.4	$\eta = 0.0107 t^{-0.779}$	0.894
0.5	$\eta = 0.0074 t^{-0.577}$	0.914
0.6	$\eta = 1.98 \times 10^{-4} e^{-2.40 \times 10^{-4} t}$	0.885
0.7	$\eta = 0.196 \times 10^{-4} e^{-1.23 \times 10^{-4} t}$	0.805
0.8	$\eta = 0.832 \times 10^{-4} e^{-1.48 \times 10^{-4} t}$	0.908
0.9	$\eta = 0.967 \times 10^{-4} e^{-2.15 \times 10^{-4} t}$	0.890
1.0	$\eta = 1.57 \times 10^{-4} e^{-2.58 \times 10^{-4} t}$	0.911

number of fine particles migrate out from the fractured mudstone in a short time, which performs the inrush mass loss, sharp decline, and rapid decline in the curves of total lost mass, mass-loss rate, and mass-migration rate, respectively. The loss-migration-ratio attenuates with time by a power function. Fractured mudstone with this continuous gradation has a high water-mud-inrush risk. For the other five Talbot power exponents of $n = 0.6$–1.0, although the fine particles migrate a lot, few fine particles are lost. It has a stable structure in the fractured mudstone, and the water-mud-inrush risk is very low.

Data availability The authors also declare that the data in this manuscript will be made available upon request.

Compliance with ethical standards

Conflict of interest The authors declare that they have no conflict of interest.

References

Chu V (2016) Mechanism on water inrush disaster of filling karst piping and numerical analysis of evolutionary process in highway tunnel. J Central South Univ (Sci Technol) 47(12):4173–4180

Chu HD, Xu GL, Yasufuku N, Yu Z, Liu PL, Wang JF (2017) Risk assessment of water inrush in karst tunnels based on two-class fuzzy comprehensive evaluation method. Arab J Geosci 10(7):1–12

Hao YQ, Rong XL, Lu H, Xiong ZM, Dong X (2018) Quantification of margins and uncertainties for the risk of water inrush in a karst tunnel: representations of epistemic uncertainty with probability. Arab J Sci Eng 43(4):1627–1640

Herman EK, Toran L, White WB (2009) Quantifying the place of karst aquifers in the groundwater to surface water continuum: A time series analysis study of storm behavior in Pennsylvania water resources. J Hydrol 376(1):307–317

Hu H, Zhang BW, Zuo YY, Zhang CM, Wang YZ, Guo Z (2018) The mechanism and numerical simulation analysis of water bursting in filling karst tunnel. Geotech Geol Eng 36:1197–1205

Hubei Hu-Rong-Xi Expressway Construction Headquarters (2009) The research of geological disaster control in high risk karst tunnel. Hubei Hu-Rong-Xi Expressway Construction Headquarters, Wuhan

Kong HL, Wang LZ (2018a) The mass loss behavior of fractured rock in seepage process: the development and application of a new seepage experimental system. Ad Civ Eng 7891914:1–12

Kong HL, Wang LZ (2018b) Seepage problems on fractured rock accompanying with mass loss during excavation in coal mines with karst collapse columns. Arab J Geosci 11(19):1–13

Li TZ, Yang XL (2018) Risk assessment model for water and mud inrush in deep and long tunnels based on normal grey cloud clustering method. KSCE J Civ Eng 22(5):1991–2001

Li LP, Li SC, Chen J, Li JH, Xu ZH, Shi SS (2011) Construction license mechanism and its application based on karst water inrush risk evaluation. Chin J Rock Mech Eng 30(7):1345–1355

Li SC, Zhou ZQ, Li LP, Shi SS, Xu ZH (2013) Risk evaluation theory and method of water inrush in karst tunnels and its applications. Chin J Rock Mech Eng 32(9):1858–1867

Li LP, Lei T, Li SC, Xu ZH, Shi SS (2015a) Dynamic risk assessment of water inrush in tunnelling and software development. Geomech Eng 9(1):57–81

Li LP, Lei T, Li SC, Zhang QQ, Xu ZH, Shi SS, Zhou ZQ (2015b) Risk assessment of water inrush in karst tunnels and software development. Arab J Geosci 8(4):1843–1854

Li TC, Lyu LX, Duan HL, Chen W (2016) Water burst mechanism of deep buried tunnel passing through weak water-rich zone. J Central South Univ (Sci Technol) 47(10):3469–3476

Li LP, Chen DY, Li SC, Shi SS, Zhang MG, Liu HL (2017a) Numerical analysis and fluid-solid coupling model test of filling-type fracture water inrush and mud gush. Geomech Eng 13(6):1011–1025

Li SC, Wu J, Xu ZH, Li LP (2017b) Unascertained measure model of water and mud inrush risk evaluation in karst tunnels and its engineering application. KSCE J Civ Eng 21(4):1170–1182

Li SC, Wu J, Xu ZH (2018) Escape route analysis after water inrush from the working face during submarine tunnel excavation construction. Mar Georesour Geotechnol 37(4):379–392

Liang DX, Jiang ZQ, Zhu SY, Sun Q, Qian ZW (2016) Experimental research on water inrush in tunnel. Nat Hazards 81(1):467–480

Liu JQ, Chen WZ, Yang DS, Yuan JQ, Li XF, Zhang QY (2017a) Nonlinear seepage-erosion coupled water inrush model for completely weathered granite. Mar Georesour Geotechnol 36(4):484–493

Liu JQ, Yang DS, Chen WZ, Yuan JQ, Li CJ, Qi XY (2017b) Research on particle starting velocity in the expansion of water inrush channel in completely weathered granite. Rock Soil Mech 38(4):1179–1187

Liu JQ, Chen WZ, Liu TG, Yu JX, Dong JL, Nie W (2018) Effects of initial porosity and water pressure on seepage-erosion properties of water inrush in completely weathered granite. Geofluids 4103645:1–11

Pan DD, Li SC, Xu ZH, Li LP, Lu W, Lin P (2018) Model tests and numerical analysis for water inrush caused by karst caves filled with confined water in tunnels. Chin J Geotec Eng 40(5):828–836

Peng YX, Wu L, Su Y, Zhou RF (2016) Risk prediction of tunnel water or mud inrush based on disaster forewarning grading. Geotech Geol Eng 34(6):1923–1932

Qian QH (2012) Challenges faced by underground projects construction safety and countermeasures. Chin J Rock Mech Eng 31(10):1945–1956

Shi SS, Xie XK, Bu L, Li LP, Zhou ZQ (2018) Hazard-based evaluation model of water inrush disaster sources in karst tunnels and its engineering application. Environ Earth Sci 77(4):1–13

Wang LZ, Kong HL (2017) Accelerated experimental study on permeability for broken rock accompanying with mass loss. The Science Publishing Company, Beijing

Wang LZ, Kong HL (2018) Variation characteristics of mass-loss rate in dynamic seepage system of the broken rocks. Geofluids 7137601:1–17

Wang DM, Zhang QS, Zhang X, Wang K, Tan YH (2016a) Model experiment on inrush of water and mud and catastrophic evolution in a fault fracture zone tunnel. Rock Soil Mech 37(10):2851–2860

Wang K, Li SC, Zhang QS, Zhang X, Li LP, Zhang QQ, Liu C (2016b) Development and application of new similar materials of surrounding rock for a fluid-solid coupling model test. Rock Soil Mech 37(9):2521–2533

Wang YC, Yin X, Jing HW, Liu RC, Su HJ (2016c) A novel cloud model for risk analysis of water inrush in karst tunnels. Environ Earth Sci 75(22):1–13

Wang LZ, Chen ZQ, Kong HL (2017a) An experimental investigation for seepage-induced instability of confined broken mudstones with consideration of mass loss. Geofluids 3057910:1–12

Wang YC, Yin X, Geng F, Jing HW, Su HJ, Liu RC (2017b) Risk assessment of water inrush in karst tunnels based on the efficacy coefficient method. Polish J Environ Stud 26(4):1765–1775

Wu J, Li SC, Xu ZH (2017) Flow characteristics and escape-route optimization after water inrush in a backward-excavated karst tunnel. Int J Geomech 17(4):1–16

Wu J, Li SC, Xu ZH, Pan DD (2018) Flow characteristics after water inrush from the working face in karst tunneling. Geomech Eng 14(5):407–419

Yang XL, Zhang SS (2018) Risk assessment model of tunnel water inrush based on improved attribute mathematical theory. J Central South Univ 25(2):379–391

Yang WM, Wang H, Yang X, Zhang B, Yang L, Fang ZD, Wang MX (2017) Development and application of model test system for water inrush in high-geostress and high hydraulic pressure tunnels. Chin J Rock Mech Eng 36(S2):3992–4001

Yuan YC, Li SC, Zhang QQ, Li LP, Shi SS, Zhou ZQ (2016) Risk assessment of water inrush in karst tunnels based on a modified grey evaluation model: sample as Shangjiawan Tunnel. Geomech Eng 11(4):493–513

Zhang QS, Wang DM, Li SC, Zhang X, Tan YH, Wang K (2017) Development and application of model test system for inrush of water and mud of tunnel in fault rupture zone. Chin J Geotech Eng 39(3):417–426

Zhao YL, Zhang LY (2018) Experimental study on the mud-water inrush characteristics through rock fractures. Ad Civ Eng 2060974:1–7

Zhou ZQ, Li SC, Li LP, Shi SS, Xu ZH (2015a) An optimal classification method for risk assessment of water inrush in karst tunnels based on grey system theory. Geomech Eng 8(5):631–647

Zhou Y, Li SC, Li LP, Shi SS, Zhang QQ, Chen DY, Song SG (2015b) 3D fluid-solid coupled model test on water-inrush in tunnel due to seepage from filled karst conduit. Chin J Rock Mech Eng 34(9):1739–1749

Zhu BB, Wu L, Peng YX, Zhou WW, Chen CH (2018) Risk assessment of water inrush in tunnel through water-rich fault. Geotech Geol Eng 36(1):317–326